Reprinted from

APPLIED PHYSICS EXPRESS

Non-Conventional Characterization of Electrically Active Dopant Profiles in Al-Implanted Ge by Depth-Resolved Micro-Raman Spectroscopy

Andrea Sanson, Enrico Napolitani, Marco Giarola, Giuliana Impellizzeri, Vittorio Privitera, Gino Mariotto, and Alberto Carnera

Appl. Phys. Express **6** (2013) 042404

Applied Physics Express 6 (2013) 042404
http://dx.doi.org/10.7567/APEX.6.042404

Non-Conventional Characterization of Electrically Active Dopant Profiles in Al-Implanted Ge by Depth-Resolved Micro-Raman Spectroscopy

Andrea Sanson[1], Enrico Napolitani[2], Marco Giarola[3], Giuliana Impellizzeri[4], Vittorio Privitera[4], Gino Mariotto[3], and Alberto Carnera[1]

[1]*Dipartimento di Fisica e Astronomia, Università di Padova, Via Marzolo 8, I-35131 Padova, Italy*
[2]*CNR-IMM MATIS at Dipartimento di Fisica e Astronomia, Università di Padova, Via Marzolo 8, I-35131 Padova, Italy*
[3]*Dipartimento di Informatica, Università di Verona, Strada le Grazie 15, I-37134 Verona, Italy*
[4]*CNR-IMM MATIS at Dipartimento di Fisica e Astronomia, Università di Catania, Via S. Sofia 64, I-95123 Catania, Italy*

Received February 22, 2013; accepted March 22, 2013; published online April 11, 2013

Al-implanted Ge samples were investigated by micro-Raman spectroscopy combined with a small angle beveling technique. By means of a reverse Monte Carlo procedure, the concentration profiles of the electrically active dopant ions were determined from the Raman peak observed at ~370 cm^{-1} related to substitutional Al atoms. Furthermore, a clear relationship between the Ge–Ge Raman peak at ~300 cm^{-1} and the active dopant concentration was also observed. This work shows that micro-Raman spectroscopy could be adopted for quantitative characterizations of the carrier concentration profiles in extrinsic semiconductors. © 2013 The Japan Society of Applied Physics

Carrier transport properties are of primary importance in improving the efficiency of semiconductor devices. In this regard, different methods and techniques are used to get information on the electrical properties of doped semiconductors.[1)] Among these, spreading resistance profiling (SRP) allows us to determine the carrier concentration profile of dopant atoms by measuring the spreading resistance vs depth on a beveled sample surface.[2)]

Micro-Raman spectroscopy is largely employed for the analysis of semiconductor devices, including strain characterization, local crystal orientation, and local temperature detection in devices under operational conditions.[3–5)] For high doping levels, it is known that the first-order Raman spectrum can be heavily affected by the carrier concentration.[6)] For example, O'Reilly et al.[7)] reported a relationship between the Si Raman shift and peak carrier concentration, measured by the Hall technique, in Sb-implanted Si. Shortly after, by combining micro-Raman spectroscopy and a small-angle beveling technique in highly p-doped Si, Becker et al.[8)] found, in the framework of the Fano resonance model,[9)] a rough relationship between the free hole concentration and the reciprocal Fano symmetry parameter of the Si Raman peak. Most recently, Perova and co-workers,[10,11)] studying the structural damage in germanium wafers caused by hydrogen and helium implants, obtained a partial correlation between SRP analysis and Raman mapping measurements. All these works show the promising potential of micro-Raman spectroscopy for the study of the concentration profiles of dopant ions. However, up to now, depth-resolved Raman scattering was not exploited in this kind of characterization, because a defined quantitative relation between Raman spectra and carrier concentration profiles is still lacking. In this Letter, micro-Raman spectroscopy has been used to quantitatively evaluate the profiles of substitutional dopant atoms and, therefore, the carrier concentration profiles. Although the method still has room for improvement, this work can be considered an important starting point for profile characterizations by Raman spectroscopy.

Ge wafers implanted with Al, which underwent post-implantation thermal annealing, have been investigated by micro-Raman spectroscopy combined with a small-angle beveling technique. Among the p-type dopants in Ge, aluminum could have a crucial place in MOSFET technology thanks to its high solid solubility.[12)] Despite this, Al has been studied on only a few occasions.[13–15)] Ge Czochralski (100)-oriented wafers, n-type Sb-doped having a resistivity higher than 40 Ω·cm (i.e., $<1 \times 10^{14}$ Sb/cm^3), were implanted with 25 keV Al^+ at a fluence of 1×10^{15} Al/cm^2 (projected range ~25 nm). After implantation, the samples were annealed in N_2 atmosphere, using a conventional furnace, at 400 °C for 1 h to induce the recrystallization of the Ge matrix by solid-phase epitaxy (SPE). Successively, two regrown samples were annealed for 1 h, one at 600 and one at 700 °C. According to Impellizzeri et al.,[15)] at 600 °C, Al shows negligible diffusion and high electrical activation, whereas at 700 °C, Al shows significant diffusion towards the bulk and unexpected uphill diffusion near the surface, together with significant electrical deactivation.

In our experiment, polarized micro-Raman spectra were collected at room temperature in backscattering geometry using a microprobe setup (Horiba-Jobin-Yvon Labram-HR, modified), mounting a holographic grating having 1800 lines/mm and equipped with a charge-coupled-device detector, cooled by liquid nitrogen. The spectra were excited by the 632.8 nm line of a mixed He–Ne gas laser focused onto a spot of about 2 μm in diameter through the lens of a 100× Olympus microscope objective (N.A. = 0.90) interfaced with a color TV camera. The laser power at the exit of the objective was about 5 mW to avoid thermal heating and the spectral resolution was about 0.3 cm^{-1}. Similarly to Refs. 10 and 11, to depth-resolve the Raman signal the samples were beveled at small angles (α) ranging (depending on the sample) from 0.33 to 0.41°. Line mapping measurements were performed along the maximum gradient direction of the beveled surface using an x–y micromovement stage, spanning more than 50 μm at steps of 0.2–0.3 μm, which corresponds, according to the relation $d = x\tan(\alpha)$, to a depth region from 0 to about 300 nm with steps of about 1.4–1.7 nm.

Typical micro-Raman spectra recorded from the sample surface, specifically in the unbeveled region, are displayed in Fig. 1. The spectra show an intense peak at about 300 cm^{-1}, due to the expected longitudinal optical phonon-mode of germanium with F_{2g} symmetry, and a weak peak at about 370 cm^{-1}. This latter can be attributed to the local vibrational mode of substitutional Al atoms in Ge on the basis of the following arguments.

i) The frequency of the vibrational local mode of a substitutional atom can be estimated using the simplified

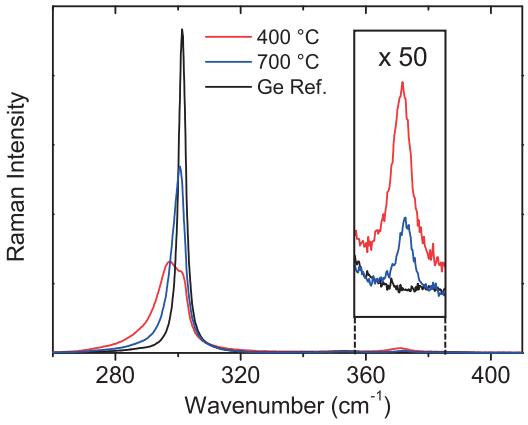

Fig. 1. Raman spectra in samples annealed at 400 °C (red lines), 700 °C (blue lines), and in pure germanium (black lines, here reported for comparison). In the inset, the vertical scale is magnified 50 times to show the Al–Ge Raman peak at ~370 cm^{-1}.

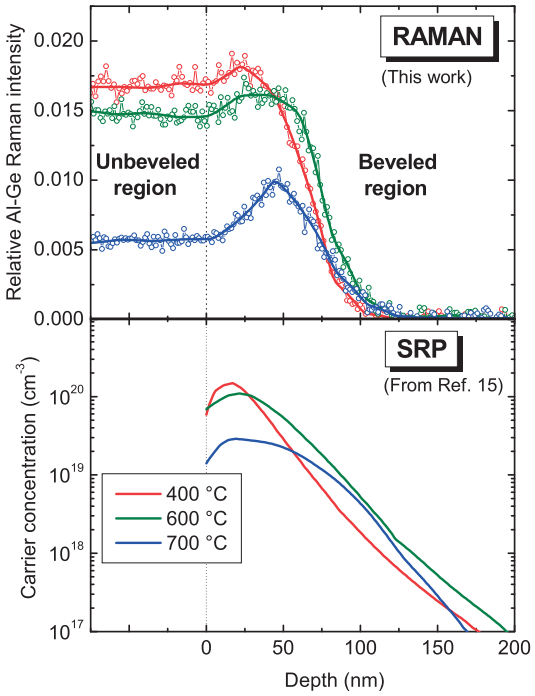

Fig. 2. Raman intensity profiles of the Al–Ge peak at ~370 cm^{-1} (top panel) and carrier concentration profiles from SRP (bottom panel). Red, green, and blue colors refer to the samples annealed at 400, 600, and 700 °C, respectively. In the top panel, each dot corresponds to the intensity measured from a single Raman spectrum, while the solid lines are the corresponding fitting curves obtained by the method described in the text.

mass-defect secular equation[16,17] that, in the case of Al in Ge, becomes $\nu_{Al} = \nu_{Ge}\sqrt{0.65 + 0.35 m_{Ge}/m_{Al}} \simeq 379\,\mathrm{cm}^{-1}$, where $\nu_{Ge} \simeq 300\,\mathrm{cm}^{-1}$ and $m_{Ge}/m_{Al} \simeq 2.69$. Although this simplified model assumes that the force constants are the same for the Al–Ge and Ge–Ge pairs, the predicted frequency, about 379 cm^{-1}, is very close to our experimental value, about 370 cm^{-1}, thereby supporting our claim.

ii) The Raman scattering tensor of the Ge–Ge mode at ~300 cm^{-1} is

$$\alpha(F_{2g}) = \begin{pmatrix} 0 & a & a \\ a & 0 & a \\ a & a & 0 \end{pmatrix}, \qquad (1)$$

therefore, in backscattering geometry, with θ indicating the angle between the electric field direction (X) of the incident light and one of the two crystallographic axes of the wafer surface, the intensity of the Raman Ge–Ge peak changes as $\sin^2(2\theta)$ for Raman measurements in parallel (XX) polarization and as $\cos^2(2\theta)$ for measurements in crossed (XY) polarization. By suitable polarized micro-Raman measurements, the Raman peak at ~370 cm^{-1} was observed to obey the same polarization selection rules as the Ge–Ge peak at ~300 cm^{-1}. Therefore, since the local symmetry is preserved, the Al–Ge peak at ~370 cm^{-1} can be definitively attributed to a local vibrational mode of substitutional Al atoms.

In order to maximize the intensity of the Raman peaks at ~300 and ~370 cm^{-1}, all the Raman spectra were collected in parallel (XX) polarization and a suitable orientation of the samples, i.e., forming an angle $\theta = 45°$ between the crystallographic axis, perpendicular to the (010) or (001) plane, and the electric field direction of incident laser radiation. The top panel of Fig. 2 shows the intensity of the Al–Ge Raman peak (i.e., the peak area, after a linear background subtraction, between 360 and 380 cm^{-1}), normalized to the intensity of the neighboring Ge–Ge peak at ~300 cm^{-1}, plotted vs the depth beneath the sample surface (right side of the figure, beveled region). The intensity of the Al–Ge Raman peak recorded from the unbeveled region, expected to be independent of the spot position, is shown on the left side of the same figure. The bottom panel of Fig. 2 displays the carrier concentration profiles obtained from SRP measurements.[15]

At this stage, a direct quantitative comparison between the two panels cannot be made because, differently from SRP, which allows us to determine the carrier concentration at the sample surface, Raman scattering probes up to some tens of nanometers beneath the sample surface. Despite this, the two panels strongly suggest a correlation between the profile of the intensity of the Al–Ge Raman peak and that of the carrier concentration. In contrast, no similar correlation is observed with the chemical Al concentration profiles (not shown) measured by secondary ions mass spectrometry (SIMS), where, as reported in Ref. 15, uphill diffusion towards the surface occurs increasing the annealing temperature to above 600 °C.

The intensity of the Al–Ge Raman peak at a depth d from the sample surface, normalized to the intensity of the Ge–Ge Raman peak, can be written as

$$\frac{I_{Al}}{I_{Ge}}(d) \simeq K \frac{\int_{-s/2}^{+s/2}\left[\frac{1}{\sqrt{2\pi}\sigma}\exp\left(-\frac{y^2}{2\sigma^2}\right)\int_{d+y}^{+\infty} P(x)\exp\left(-\frac{x-d-y}{L/2}\right)dx\right]dy}{\int_{-s/2}^{+s/2}\left[\frac{1}{\sqrt{2\pi}\sigma}\exp\left(-\frac{y^2}{2\sigma^2}\right)\int_{d+y}^{+\infty} C_{Ge}\exp\left(-\frac{x-d-y}{L/2}\right)dx\right]dy}$$

$$= K \frac{\int_{-s/2}^{+s/2} \left[\frac{1}{\sqrt{2\pi}\sigma} \exp\left(-\frac{y^2}{2\sigma^2}\right) \int_{d+y}^{+\infty} P(x) \exp\left(-\frac{x-d-y}{L/2}\right) dx \right] dy}{C_{Ge} L/2}, \quad (2)$$

where $P(x)$ is the concentration of substitutional Al atoms at depth x beneath the unbeveled sample surface, $C_{Ge} = 4.42 \times 10^{22}$ at./cm^3 is the density of crystalline germanium (assumed to be the same in the implanted samples), K is the ratio between the Raman efficiency of the Al–Ge and Ge–Ge bonds whose value, which is unknown, can be reasonably estimated as 12 ± 3 from the fitting procedure described below. The integrals in dx take into account the optical absorption of the incident and backscattered light. From Ref. 18, the optical absorption length, L, is estimated to be ~70 nm. The integrals in dy take into account the laser intensity profile, here assumed to have a Gaussian distribution with standard deviation $D/6$, where $D \simeq 2\,\mu$m is the laser spot size. Accordingly, in Eq. (2), with α indicating the beveling angle, $s = D\tan(\alpha)$ and $\sigma = s/6 \simeq 2$–3 nm are the laser spot size and standard deviation, respectively, projected along the depth direction.

Using the expression derived above, the Raman intensity profile I_{Al}/I_{Ge} was simulated, for each sample, for an arbitrary starting $P(x)$ distribution and compared with the experimental Raman profiles displayed in Fig. 2. The distribution $P(x)$ was then varied, by means of a Monte Carlo procedure, in order to optimize the agreement between simulated and experimental Raman profiles. The resulting simulated Raman profiles are shown with solid lines in the top panel of Fig. 2, while the corresponding simulated $P(x)$ distributions are shown in Fig. 3 and compared with the carrier concentration profiles obtained by SRP measurements. The reconstructed $P(x)$ distributions of substitutional Al atoms, obtained from the intensity of the Al–Ge Raman peak, are in fairly good agreement with the carrier concentration profiles measured by SRP analysis.

The discrepancies between Raman and SRP profiles deserve to be discussed here. One of the main causes of the discrepancy is the difficulty of assessing the intensity of the Al–Ge Raman peak, because, being weak, it can be significantly altered by the background subtraction of Raman spectra. This difficulty is reflected, at least in part, by the uncertainty of the parameter K. Besides this, the optical absorption length, L, was set to be 70 nm. However, this theoretical value refers to pure Ge and, in our case, L might have a non-negligible dependence on the Al concentration. Last, but not least important, errors in the SRP measurements might contribute to the above discrepancies.

Let us now consider the Ge–Ge Raman peak at about 300 cm^{-1}. Figure 4 shows the average position and the full width at half maximum (FWHM) of the Ge–Ge Raman peak (top and bottom panels, respectively), for all the samples and pure Ge, plotted vs the depth beneath the sample surface. A similar behavior is also observed for the peak asymmetry, not shown here. The pure Ge, used as a reference, allows us to evaluate the effects of beveling on the Ge–Ge Raman peak: about 1 cm^{-1} in the average position and about 0.5 cm^{-1} in the FWHM.

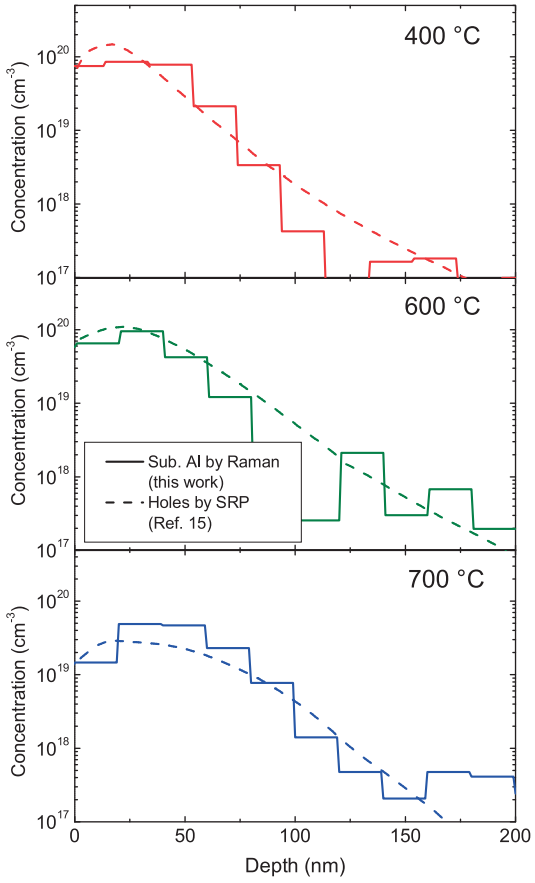

Fig. 3. Comparison between carrier concentration profiles from SRP measurements (dashed lines) and simulated profiles obtained from the Al–Ge Raman peak intensity (solid lines).

The shift and broadening of the Ge–Ge Raman peak, as evidenced by Fig. 4, can be associated with phonon confinement,[19] strain[20] or, as introduced above, to carrier concentration effects.[6] In the present case, phonon confinement effects can be disregarded since the presence of Ge nanocrystalline regions or clusters was ruled out by transmission electron microscope investigations.[15] Concerning the strain, implanted (and annealed) samples typically display a lattice strain lower than a few 0.1%, also in the case of high doping levels.[21,22] In all our Al-implanted Ge samples, high resolution X-ray diffraction showed a lattice strain profile (not reported here) lower than 0.03% in the whole depth range.[23] According to Peng et al.,[20] a Ge lattice strain of this magnitude induces much smaller effects on the Ge–Ge Raman peak than those reported in Fig. 4. As a consequence, we can conclude that the changes in the Ge–Ge Raman peak of Fig. 4 are entirely due to carrier concentration effects, as predicted in Ref. 6.

With this regard, the shift and the FWHM broadening of the Ge–Ge Raman peak were calculated with respect to pure Ge, in each sample and for each single Raman spectrum, and plotted against the corresponding intensity of the Al–Ge

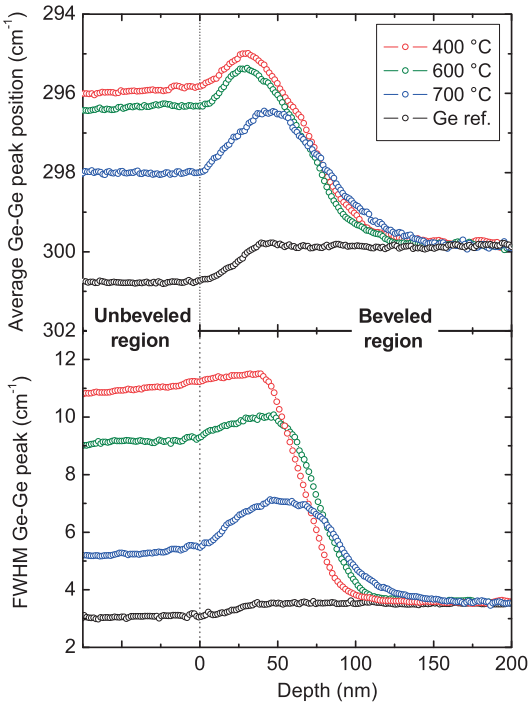

Fig. 4. Depth profiles of the average position (top panel) and FWHM (bottom panel) of the Ge–Ge Raman peak at ~300 cm^{-1}. Red, green, and blue colors refer to the samples annealed at 400, 600, and 700 °C, respectively. The black color refers to the pure Ge, used here as a reference.

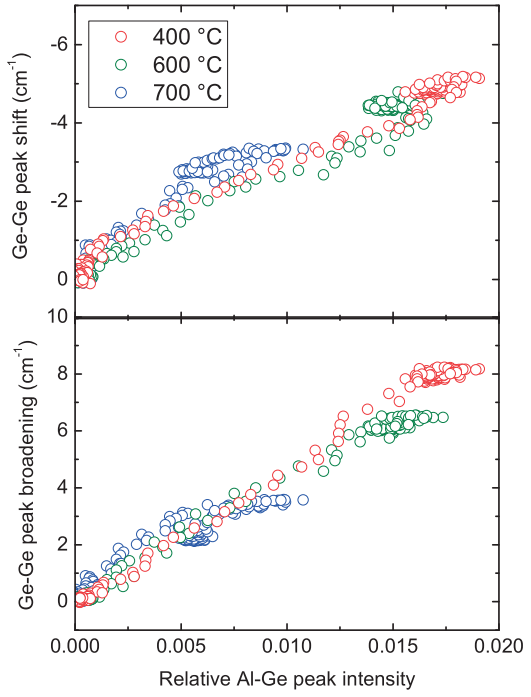

Fig. 5. Shift (top panel) and FWHM broadening (bottom panel) of the Ge–Ge Raman peak with respect to pure Ge, plotted vs the Al–Ge Raman peak intensity. Red, green, and blue circles refer to the samples at at 400, 600, and 700 °C, respectively.

Raman peak, as shown in Fig. 5. Although the ensemble of Ge–Ge Raman shifts and FWHMs, with respect to the Al–Ge peak intensity, varies in a range of ~1 cm^{-1} owing to the non-negligible uncertainty in the Al–Ge peak amplitude, the figure shows a clear relationship between the Ge–Ge Raman peak and the intensity of the Al–Ge one. This means that the Ge–Ge Raman peak could be exploited to determine the content of substitutional Al atoms and, therefore, the carrier concentration profiles in implanted Ge samples. This result should turn out especially relevant in those cases where the Raman peaks related to the local vibrational modes of substitutional dopant atoms are not detected.

In conclusion, in this work, Al-implanted Ge samples were studied by micro-Raman spectroscopy coupled to the small-angle beveling technique. By using a Monte Carlo procedure, the active dopant profiles were estimated from the intensity of the Al–Ge Raman peak due to substitutional Al atoms. Moreover, the correlation observed between the Ge–Ge Raman peak and substitutional Al content, directly related to the carrier concentration profiles, validates the possibility of adopting micro-Raman spectroscopy for dopant profile characterizations also in those cases where the Raman peaks, due to substitutional dopant atoms, are not observed. Further studies are mandatory to make the method outlined here more reliable and efficient. Nevertheless, this work might represent a breakthrough for the development of depth-resolved micro-Raman spectroscopy for quantitative characterizations of doping species profiles in Ge.

1) L. J. Van der Pauw: Philips Res. Rep. **13** (1958) 1.
2) W. Vandervorst, T. Clarysse, and P. Eyben: J. Vac. Sci. Technol. B **20** (2002) 451.
3) G. Abstreiter: Appl. Surf. Sci. **50** (1991) 73.
4) R. Ostermeir, W. Schottky, K. Brunner, G. Abstreiter, and W. Weber: IEEE Trans. Electron Devices **39** (1992) 858.
5) I. De Wolf: Semicond. Sci. Technol. **11** (1996) 139.
6) F. Cerdeira and M. Cardona: Phys. Rev. B **5** (1972) 1440.
7) L. O'Reilly, K. Horan, P. J. McNally, N. S. Bennett, N. E. B. Cowern, A. Lankinen, B. J. Sealy, R. M. Gwilliam, T. C. Q. Noakes, and P. Bailey: Appl. Phys. Lett. **92** (2008) 233506.
8) M. Becker, U. Gösele, A. Hofmann, and S. Christiansen: J. Appl. Phys. **106** (2009) 074515.
9) F. Cerdeira, T. A. Fjeldly, and M. Cardona: Phys. Rev. B **8** (1973) 4734.
10) T. S. Perova, B. M. Armstrong, J. Wasyluk, P. Baine, P. Rainey, S. J. N. Mitchell, D. W. McNeill, H. S. Gamble, and R. Hurley: Solid State Phenom. **178–179** (2011) 295.
11) J. Wasyluk, P. V. Rainey, T. S. Perova, S. J. N. Mitchell, D. W. McNeill, H. S. Gamble, B. M. Armstrong, and R. Hurley: J. Raman Spectrosc. **43** (2012) 448.
12) V. I. Fistul: *Impurities in Semiconductors: Solubility, Migration, and Interactions* (CRC Press, Boca Raton, FL, 2004) p. 157.
13) T. Itoh and I. Ohdomari: Jpn. J. Appl. Phys. **10** (1971) 1002.
14) P. Dorner, W. Gust, A. Lodding, H. Odelius, B. Predel, and U. Roll: Acta Metall. **30** (1982) 941.
15) G. Impellizzeri, E. Napolitani, S. Boninelli, V. Privitera, T. Clarysse, W. Vandervorst, and F. Priolo: Appl. Phys. Express **5** (2012) 021301.
16) G. Contreras, M. Cardona, and A. Compaan: Solid State Commun. **53** (1985) 857.
17) M. A. Renucci, J. B. Renucci, and M. Cardona: in *Light Scattering in Solids*, ed. M. Balkanski (Flammarion, Paris, 1971) p. 326.
18) D. E. Aspnes and A. A. Studna: Phys. Rev. B **27** (1983) 985. $L \simeq 70$ nm takes into account the absorption length of both incident and Raman scattered light (i.e., Stokes at ~370 cm^{-1}).
19) H. Richter, Z. P. Wang, and L. Ley: Solid State Commun. **39** (1981) 625.
20) C. Y. Peng, C. F. Huang, Y. C. Fu, Y. H. Yang, C. Y. Lai, S. T. Chang, and C. W. Liu: J. Appl. Phys. **105** (2009) 083537.
21) L. Romano, R. De Bastiani, C. Miccoli, G. Bisognin, E. Napolitani, D. De Salvador, and M. G. Grimaldi: Mater. Sci. Eng. B **135** (2006) 220.
22) G. Bisognin, S. Vangelista, M. Berti, G. Impellizzeri, and M. G. Grimaldi: J. Appl. Phys. **107** (2010) 103512.
23) E. Napolitani et al.: work in progress, unpublished.